Revision 3

Correlated Cathodoluminescence Features, Trace Element Chemistry and Geochronology of Cassiterite (SnO_2) from the World-class Gejiu Tin District, China

Yanbo Cheng [a, b] *, Carl Spandler [a], Anthony Kemp [a, c], Jingwen Mao [b], Brian Rusk [a, d], Yi Hu [e], Kevin Blake [e]

[a] *Economic Geology Research Center (EGRU), Department of Geosciences, James Cook University, Townsville, 4811, Australia*

[b] *MLR Key Laboratory of Metallogeny and Mineral Assessment, Institute of Mineral Resources, Chinese Academy of Geological Sciences, Beijing 100037, China*

[c] *Centre for Exploration Targeting (CET), School of Earth Sciences, The University of Western Australia, Perth, 6009, Australia*

[d] *Geology Department, Western Washington University, Bellingham, 98225, United States*

[e] *Advanced Analytical Centre (AAC), James Cook University, Townsville, 4811, Australia*

---

*Corresponding author.
Email address: yanbo.cheng1@jcu.edu.au

Abstract

This paper evaluates controls on cassiterite crystallization under hydrothermal conditions based on the textural setting and geochemistry of cassiterite from six different mineralization environments from the world class Gejiu tin district, SW China. The cassiterite samples feature diverse internal textures, as revealed by cathodoluminescence (CL) imaging, and contain a range of trivalent (Ga, Sc, Fe, Sb), quadrivalent (W, U, Ti, Zr, Hf), and pentavalent (Nb, Ta, V) trace elements, with Fe, Ti, and W being the most abundant trace elements. Cassiterite Ti/Zr ratios tend to decrease with distant away from the causative granite intrusion, and so has potential to be used as a broad tool for vectoring towards a mineralized intrusive system.

Elemental mapping of cassiterite grains reveals that trace element concentration variations correspond closely to CL zoning patterns. The exceptions are distinct irregular domains that sharply cut across the primary oscillatory zoning, as defined by the concentrations of W, U, Sb, and Fe. These zones are interpreted to have formed after primary cassiterite growth via fluid-driven dissolution-reprecipitation processes. Zones with low W and U (and Sb) and high Fe are interpreted to have formed during interaction with relatively oxidized fluids, in which W and U are stripped from cassiterite due to cation exchange with Fe^{3+}. Systematics of W, U, Sb, and Fe partitioning into cassiterite can therefore be used as a monitor of the relative oxidation state of the hydrothermal fluid from which cassiterite precipitates.

Cassiterite U-Pb geochronology results obtained by LA-ICP-MS return ages between 77 Ma and 83 Ma, which is consistent with previous geochronology from the region. Ages determined on zones of dissolution-reprecipitation are similar to ages for primary cassiterite growth, indicating a short (<3 m.y.) timespan of hydrothermal activity. These results confirm the potential of U-Pb dating of cassiterite for directly constraining the timing of Sn deposition.

Key words: cassiterite, cathodoluminescence (CL) imaging, trace element, fluid redox, geochronology

Introduction

Most of the world's tin mineralization is thought to be linked to hydrothermal processes associated with highly fractionated and relatively reduced granite bodies (Lehmann, 1990; Heinrich, 1990, 1995). The most important tin ore mineral is cassiterite (ideally SnO_2), which has a tetragonal lattice structure similar to that of rutile, with Sn cations in six-fold coordination with oxygen. As with rutile, cassiterite can accommodate a wide range of trace elements, including Fe, Ti, W, Ta, Nb, Mn, and Sc (Schneider et al., 1978; Moore and Howie, 1979; Fig. 1). This trace element affinity may be used to infer aspects of fluid compositions and mineralization processes, but we have an incomplete understanding of how trace elements are incorporated in cassiterite (Giuliani, 1987). Furthermore, like other quadrivalent element-loving minerals (e.g., zircon, rutile, titanite), cassiterite may incorporate U^{4+} much more strongly than Pb^{2+} (Fig. 1), which means that U-Pb dating of cassiterite may be a robust and reliable geochronometer for Sn mineralizing systems. Despite this potential, there has been relatively little comprehensive work on cassiterite geochemistry and geochronology (Gulson and Jones, 1992; Yuan et al., 2008; Zhang et al., 2015).

Cathodoluminescence (CL) is a powerful micro-imaging tool for revealing internal textures, zoning and the distribution of trace element within minerals (e.g. Rusk and Reed, 2002; Götze and Kempe, 2008). Titanium, W, Al, and V impurities are considered to be the chief activators responsible for CL in hydrothermal cassiterite, whereas Fe is considered to be a 'CL blocker', causing a lowering of CL intensity

(Farmer et al., 1991). Nevertheless, more information about cassiterite CL patterns and their possible link with chemical compositions are needed. In recent years, CL and laser ablation ICP-MS analysis have been successfully combined to correlate micro-textures and compositions of various minerals (e.g., Rusk et al., 2008; Chen and Simonetti, 2012; Hammerli et al., 2013). There is great potential to apply these techniques to cassiterite, given its demonstrated cathodoluminescent properties (Farmer et al., 1991) and potential as a trace element host (Murciego et al., 1997; Pieczka et al., 2007).

In this paper, we examine cassiterite grains from the six different ore styles from the Gejiu tin ore district of southwest China. These mineralization styles provide an excellent sample suite to compare and contrast the chemical and physical characteristics of cassiterite formed in different ore environments. Based on CL imaging, EPMA analysis and LA-ICP-MS analysis (for trace elements and U-Pb isotopes), we report; (i) concentration data for an extensive set of trace elements in cassiterite; (ii) elemental zoning in cassiterite formed during primary crystallization and subsequent dissolution-reprecipitation processes; (iii) correlation between micro-textures and trace elements in cassiterite, and; (iv) robust cassiterite U-Pb age data determined by LA-ICP-MS. These results provide further insights into ore genesis in the world-class Gejiu tin district, and also highlight the potential of using cassiterite as a monitor of hydrothermal processes and for understanding the timing and evolution of Sn mineralization events.

Geological Background

The Gejiu tin polymetallic ore district represents the largest primary tin accumulation in the world, with an endowment estimated at ~10 million metric tonnes (Mt) of Sn-Cu-Pb-Zn ore (308 Geological Party, 1984; Zhuang et al., 1997). The Gejiu District is located on the western margin of the South China Block, adjacent to the Yangtze Craton in the north and the Three Rivers Fold Belt in the west. The geology of the Gejiu area consists largely of the Middle Triassic Gejiu Formation carbonate sequences and Middle Triassic Falang Formation, which consists of fine-grained clastic and carbonate sediments with intercalated mafic lavas (Fig. 2). The Gejiu Batholith is composed of gabbro, porphyritic and equigranular biotite granites, syenites, and mafic dykes (Fig. 2; see also Cheng et al., 2012). Mineralization in the Gejiu mining district comprises five Sn-Cu-Pb-Zn polymetallic deposits, which − from north to south − are named Malage, Songshujiao, Gaosong, Laochang, and Kafang. The multiple mineralization styles are characterized by extensive hydrothermal alteration and clear metal zoning around granitic cupolas (Fig. 2; 308 Geological Party, 1984). Recent studies have revealed that the Gejiu granite batholith was emplaced between 85 Ma and 77 Ma (Fig. 2; Cheng and Mao, 2010), which is consistent with the Re-Os and ^{40}Ar-^{39}Ar ages (between 86 Ma and 77 Ma) of various ores in the district (Fig. 2; Cheng, 2012).

Tin mineralization in the Gejiu area occurs as 6 ore styles: (1) tin granite ores; (2) greisen ores; (3) skarn ores; (4) carbonate-hosted vein-type ores; (5) oxidized ores and; (6) semi-oxidized stratiform ores (Appendix 1-1). Cassiterite-bearing granite is not common in the ore district and is only well developed in the interior of certain granite cupolas. Cassiterite hosted by tin granite is always intergrown with fluorite and accompanied by tourmaline. Greisen ores are not common in the region and mainly consist of muscovite and quartz, with fluorite and tourmaline locally observed. Cassiterite, scheelite, chalcopyrite, and pyrrhotite are the major greisen ore minerals. Skarn-related ores are widely distributed across the ore district and are the most economically important mineralization style. The skarns are pyroxene- and garnet-rich with associated tremolite, actinolite, epidote, chlorite, fluorite, and tourmaline. The major ore minerals are cassiterite, pyrrhotite, and chalcopyrite. Vein-type ores have only been discovered in the Dadoushan area of the Laochang deposit (Fig. 2 and Appendix 1-1); these ores contain skarn minerals (garnet, pyroxene, epidote, and fluorite) and tourmaline. Observable ore minerals in vein-type mineralization include cassiterite, chalcopyrite, pyrrhotite, scheelite, and beryl (Cheng, 2012). The oxidized stratiform style ores are products of the oxidation of primary sulfide ores. These are mainly developed between carbonate layers distal to granite (Appendix 1-1), and are dominated by hematite and limonite. Some incompletely oxidized ores in the oxidized stratiform orebodies contain hematite, limonite, pyrrhotite, and minor pyrite (semi-oxidized ores), most of which are close to the surface and associated with small-scale faults (Appendix 1-1).

Sampling Strategy

Cassiterite samples were collected from the six different ore-forming environments of the Gaosong deposit, Gejiu district (Appendix 1-1). The samples were collected along a vertical traverse from close to the granitic pluton (i.e., the tin granite ore, sample no. A0374-1), greisen (sample no. A0374-7), skarn (sample no. A0374-3), semi-oxidized (sample no. A0374-9), oxidized (sample no. A0374-11) to vein ore (sample no. A0374-6). Examination of ore samples along this traverse presents the opportunity to observe how cassiterite micro-textures, trace-element composition and crystallization age vary in different environments in a spatially evolving hydrothermal system. A brief outline of these samples is given below, and in Appendix 1-1 and Table 1.

Sample A0374-3 represents cassiterite that occurs in granite located on the upper interior margin of ore-related granite cupolas (Appendix 1-1). These rocks represent the last intrusive stage of the highly evolved granite. Major minerals include K-feldspar, plagioclase, and quartz, with accessory muscovite, fluorite, tourmaline, and cassiterite (Figs. 3 and 4). Mafic minerals, such as biotite and amphibole, are not observed. Sample A0374-7 represents greisen ore, which is produced from the interaction of greisen-forming fluids with granite at the margins the pluton (Appendix 1-1), and mainly contains quartz and muscovite with minor tourmaline, fluorite, and cassiterite (Fig. 3). A0374-1 is a skarn ore that formed by the interaction of granite-derived fluids with carbonate rocks near the margin of the granite (Appendix 1-1). The sample contains garnet, pyroxene, tremolite, chlorite, epidote, tourmaline and calcite (for more details, see Cheng et al., 2013). Samples A0374-9 and A0374-11 were collected from the stratiform oxidized ores and semi-oxidized ores, respectively

(Appendix 1-1). Major minerals of oxidized ores include hematite, hydrohematite, and minor limonite, hydrogoethite, plumbojarosite, minetisite, cassiterite, malachite, and cerussite, while the semi-oxidized ore contains limonite, goethite, pyrite, arsenopyrite, galena, marmatite, chalcopyrite, and cassiterite (for more details see Cheng et al., 2015). Sample A0374-6 represents cassiterite from vein ores, which is extensively developed in shallow surface of the Dadoushan open pit (Cheng, 2012). The most common mineral is tourmaline, accompanied by skarn minerals (garnet, diopside, epidote, phlogopite) and beryl. Cassiterite is the main ore mineral, accompanied by minor chalcopyrite, pyrrhotite, and pyrite, as well as scheelite

Analytical Methods

Cassiterite grains examined in this study were separated from ~2 kg bulk ore samples, using conventional rock crushing down to 200 µm, followed by heavy liquid and magnetic separation techniques. Cassiterite grains were then handpicked under a binocular microscope, mounted in epoxy resin, and polished. The mounts were photographed in transmitted and reflected light, and then the cassiterite grains were studied for internal structure, trace element composition, and U-Pb geochronology using cathodoluminescence (CL), electronprobe microanalysis (EPMA), and laser ablation ICP-MS techniques.

SEM-CL

Cathodoluminescence (CL) and backscattered electron (BSE) images of cassiterite were obtained from carbon-coated epoxy resin mounts using a JEOL JSM5410LV scanning electron microscope (SEM), fitted with a Robinson CL detector, at the Advanced Analytical Centre, James Cook University (JCU), Australia. BSE and CL images were acquired at 20 kV acceleration voltage, with a current of 6 nA and a focused electron beam using the JEOL Semafore digital image acquisition software.

EPMA

X-ray element maps of cassiterite were acquired by electron microprobe using a JEOL JXA 8200 electron microprobe at the Advanced Analytical Centre, JCU. Element mapping of Sn, W, Fe, Ti, and Nb were carried out by wavelength dispersive spectrometry (WDS) with a focused beam operating at conditions of 200 nA beam current and 15 kV accelerating voltage. The stage step distance was between 1 and 4 µm (depending on the given area to be mapped) and the dwell time per point was set to 100 ms.

Laser ablation ICP-MS trace element analysis

All laser ablation ICP-MS analyses were conducted at the Advanced Analytical Centre, JCU, using a Coherent GeolasPro 193 nm ArF Excimer laser ablation system connected to a Bruker 820-MS (formerly Varian 820-MS) ICP-MS. The ablation cell was connected to the ICP-MS via Tygon tubing and a plastic Y-piece. The standard cylindrical sample cell was used throughout the study, but with a custom-designed polycarbonate insert to reduce the effective volume to 4 cm^3. This insert provides rapid signal washout of about 1.2 s. The ICP-MS was tuned to ensure robust plasma conditions (U/Th sensitivity ratio ~1) while maintaining low oxide production rate (ThO/Th ratio is greater than 0.5 %). The laser beam diameter and repetition rate were set 60 μm, and 10 Hz, respectively, and laser energy density at the sample site was set to 6 J/cm^2. NIST 612 glass standard was used as the bracketing external standard, using the reference values of Spandler et al. (2011). ^{119}Sn was used as the internal standard, assuming stoichiometric SnO_2 for quantification purposes. Data were processed using the GLITTER software (van Achterbergh et al., 2001).

Trace element LA-ICP-MS mapping on cassiterite was carried out using Step&Repeat Mode and a 16 μm diameter beam size. Mapping starts from the bottom of the area to be mapped and each line was scanned in a single direction from right to left. The sample was oriented so that the scan line was perpendicular to the carrier gas He nozzle in order to minimize sampling material redeposited from previous ablation. NIST 612 glass was used for external standardization and Sn was used for internal standardization.

Laser ablation ICP-MS U-Pb geochronology

Uranium-Pb geochronology data were generated with the LA-ICP-MS instrumentation described above. The measured isotopes were (dwell times in parenthesis), ^{29}Si (10 ms), ^{119}Sn (10 ms), ^{204}(Pb+Hg, 20 ms), ^{206}Pb (30 ms), ^{207}Pb (30 ms), ^{208}Pb (20 ms), ^{232}Th (30 ms), ^{235}U (30 ms), and ^{238}U (30 ms). The total analysis time was 65 s, of which the first 30 s was used as a gas blank (laser firing, shutter closed).

It is well established that matrix-matching of samples and standards is highly desirable for accurate U-Pb isotope results by laser ablation ICP-MS. Unfortunately, well-characterized cassiterite reference materials for U-Pb dating are currently not available, and this presents a significant obstacle for the present study. Our strategy to minimize this uncertainty involved tuning the laser parameters and ICP-MS so that the down-hole Pb/U fractionation profile obtained from cassiterite matched, as closely as possible, that from the silicate glass standard NIST 612. We found that this was best achieved using large spot diameters (44-58 µm), laser fluence of 4 J/cm^2, and by tuning the ICPMS so that the $^{206}Pb/^{238}U$ ratio obtained from NIST 610 glass at the start of ablation was similar to the reference value (~0.22; see Tucker et al., 2013). Under these optimized conditions, Pb/U ratios in cassiterite and NIST 612 glass define similar time resolved trends with minimal in-run Pb/U fractionation (Appendix 2-1). This implies that NIST 612 glass is suitable as a standard to calibrate Pb/U ratios in cassiterite. Note that the larger and non-linear down-hole Pb/U fractionation trend produced by zircon under these conditions means that this mineral could not be used to successfully standardize Pb/U ages from cassiterite (Appendix 2-1). Our reconnaissance analysis of cassiterite from our samples also revealed high and consistent ^{238}U and ^{206}Pb signals, that have parallel evolution in the time-resolved spectra, whereas common Pb (^{204}Pb) contents are usually negligible (at background levels) (Appendix 2-2); these are desired criteria of in-situ U-Pb dating by laser ablation ICP-MS. As a test of this procedure, we analysed cassiterite hosted by a Carboniferous tin granite of the Herberton area, north Queensland, where U-Pb ratios are calibrated against bracketing analyses of NIST 612 glass. We obtained a ^{206}Pb/^{238}U age of 318 ± 2 Ma (see details in Appendixes 2-3 and 2-4), which is consistent with previously determined ages of Sn mineralization in this area of 320.± 3 Ma and 317.± 3 Ma (see Cheng et al., 2018). This result demonstrates that the method described above is capable of producing precise and accurate Pb/U ages from cassiterite.

Data reduction in this study was carried out using the software 'GLITTER' (van Achterbergh et al., 2001). Time-resolved isotope signals from cassiterite samples and bracketing analyses of NIST 612 glass were filtered for spikes or perturbations related to inclusions and fractures. Age calculations and U-Pb concordia plots were made with Isoplot Ex (Ludwig, 2003). Although most analyses contain low common Pb (as revealed by low levels of ^{204}Pb; Appendix 2-2) and plot close to concordia, some analyses were highly discordant, and hence are assumed to contain a component of common Pb. Therefore, age calculations are made by projecting a line of best fit through the uncorrected data on a Tera-Wasserburg Concordia plot. The lower intercept is taken to represent the crystallisation age of cassiterite, as is common practice for dating common Pb-bearing minerals (Chew et al., 2014). The upper intersect on concordia is at ^{207}Pb/^{206}Pb values of between 0.8-0.9, which is broadly consistent with the primordial Pb isotope composition of Stacey and Kramers (1975).

Results

Micro-texture and crystal size variations

Cathodoluminescence images effectively reveal the internal microtextures of cassiterite from different mineralization environments in Gejiu district (Fig. 5). Cassiterite crystals from all mineralization styles can be categorized into two groups based on their size, shape, and CL zoning features. In general, cassiterite grains from tin granite, greisen, and skarn ores are relatively large, about 400 × 600 µm in size, and are characterized by euhedral, micrometer-scale oscillatory zoning (Fig. 5). In contrast, cassiterite grains from semi-oxidized ores, stratiform oxidized ores and veins tend to be smaller (ca. 50 × 200 µm in size), anhedral and have irregular and relatively complex zoning patterns (Fig. 5). Some cassiterite grains from these ore types are highly luminescent while others appear dark in CL (weak or no CL response), and other crystals display irregular variations between bright and dark CL (Fig. 5). Grains from the oxidized and semi-oxidized ore samples often have domains with fine oscillatory zoning truncated or overgrown by zones with dark or diffuse CL signature.

In most cases, internal zoning in cassiterite grains revealed by BSE images correlate with zoning patterns evident in the CL images, indicating that the variations in CL signals are due to intra-grain scale compositional variations. The cassiterite grains are largely free of inclusions with the exception of occasional micron-sized inclusions of scheelite, Fe-oxide and native bismuth.

Trace element mapping

Trace-element mapping results show a direct relationship between element distribution and CL-defined zoning in all samples examined. Here, we discuss one sample of greisen ore (A0374-1) in detail as an example. Element maps of the cassiterite grain show that the distribution of Nb, Ta, and Ti correlates with the regular and continuous oscillatory zoning pattern displayed by CL and BSE images (Fig. 6). In detail, there appears to be a direct correlation between Nb and Ta concentrations, but no direct correlation with Ti content. The distributions of Fe, W and U express complex and partly cryptic zonation patterns. Although aspects of the oscillatory zoning evident in CL are present in the Fe, W and U distribution maps, the more prominent feature of these maps are irregular zones of contrasted element concentration that are highly discordant to the oscillatory zoning (Fig. 6). This second zoning style appears to have no geometric relationship with either the oscillatory growth zoning or the crystal surface, but there is an antipathic relationship in the concentration of Fe (and to some extent Sc) compared to W and U (and Sb). In other words, the Fe-rich zones are W- and U-depleted, and vice versa.

Trace element composition

The most abundant trace elements in the analyzed cassiterites are Ti (3 to >5000 ppm), Fe (35 to >6500 ppm), and W (<1 to >8000 ppm). Niobium and Ta concentrations also vary significantly, from <0.01 ppm up to ~1800 ppm (in vein sample) for Nb, and up to ~500 ppm (in greisen sample) for Ta. Concentrations of other elements also vary over several orders of magnitude, even within a single sample of an ore type (e.g., W and U). Aluminium, Sc, V, Ga, Cr, Zr, and Sb concentrations are mostly below 50 ppm (Appendix 3). Elements that were consistently determined to be close to, or below detection limits include Ca, Cu, Zn, Mo, Rb, Sr, Th, and REE. Uranium contents are below 40 ppm and Hf concentration are generally below 5 ppm. There are clear positive correlations between Nb and Ta, Zr and Hf, V and Sc, W, and U, and most trivalent elements (Ga, Fe, Sc, Al) in the cassiterite samples, as shown in Figs. 7 and 8.

In general, cassiterite from tin granite, greisen, and skarn ores contain higher Al, V, and Ti contents, but lower Mn, than cassiterite from the semi-oxidized and oxidized samples (Appendix 3). The skarn ore cassiterite has the highest Sc and V contents (Fig. 8E). The greisen samples tend to have the highest Hf and Ta contents, and hence relatively low Zr/Hf and Nb/Ta. Zr/Hf ratios vary between samples, from ~12.5 for the greisen ore, to ~67 for the vein ore (Fig. 7B). There is considerable intra-grain variability in Ti/Zr (Fig. 7C), but overall we observe a decrease in Ti/Zr of cassiterite from the tin granite sample (most proximal to the causative intrusion) out to the vein ore sample (most distal ore from the intrusion). The vein and oxidized ore samples show the largest concentration ranges for most elements, but overall have the lowest Ti, Al, V, Sc and (for the oxidized ore) Nb and Ta contents. In contrast, the oxidized ore cassiterite has distinctly elevated Ga and Fe contents (Fig. 8F).

Results from the spot analyses confirm the general elemental associations revealed by the element distribution maps (Fig. 6). In particular, the two distinct compositional domains based on W, U, and Fe distribution are evident for the tin granite, greisen, and skarn ore cassiterite (Fig. 8A, B). Antimony is the only other element that correlates with W and U (Fig. 8C). Ore samples that are distal to the granite intrusion (oxidized, semi-oxidized, and vein) show similar broad correlations between W, U, and Fe, although for these ores there is considerably more scatter in the concentration data, and no distinct compositional domains are recognized (Fig. 8A-C).

LA-ICP-MS U-Pb dating

We undertook U-Pb isotope analyses for dating of the 6 samples of cassiterite, including analyses of both compositional domains where present (tin granite, greisen, and skarn ore). The final age is calculated from the $^{206}Pb/^{238}U$ intercept ages of the selected grains at 95% confidence level. Uranium-Pb datasets and concordia diagrams are presented in Appendix 4 and Figure 9, respectively.

Eight analyses on the high W+U, low Fe domain and 16 analyses on low W+U, high Fe domain from the tin granite sample (A0374-3) yielded ages of 81.1 ± 1.3 Ma (MSWD = 3.1), and 81.5 ± 2.3 Ma (MSWD = 4.0), respectively (Fig. 9).

Twenty two analyses performed on greisen ore sample A0374-7 cassiterite gave $^{206}Pb/^{238}U$ ages of 80.8 ± 1.0 Ma (MSWD = 2.1) for the high W+U, low Fe domain (11 analyses), and 81.5 ± 0.5 Ma (MSWD = 1.4) for the low W+U, high Fe domain.

Skarn ore cassiterite (sample A0374-1) yielded a U–Pb age of 76.4 ± 1.7 Ma (MSWD = 0.2) for the high W+U, low Fe domain (3 analyses), and 77.9 ± 1.2 Ma

(MSWD = 0.6) for the low W+U, high Fe domain (10 analyses).

Distinct compositional domains were not recognized in the 3 distal ore samples, so only a single age was determined for each of these samples. Twenty analyses each of semi-oxidized, oxidised and vein ore cassiterite yielded concordia intercept ages of 78.8 ± 1.3 Ma, 81.9 ± 1.4 Ma, and 83.6 ± 1.3 Ma respectively (MSWD of 3.1, 2.8, and 2.0 respectively).

Discussion

Controls on trace element variations in cassiterite

According to conditions of charge, radius, and coordination of ions compared with Sn^{4+} in cassiterite (Fig. 1), we consider the following elements likely to be compatible in cassiterite: Fe^{3+}, Ga^{3+}, V^{3+}, Cr^{3+}, Sc^{3+}, Sb^{3+}, W^{4+}, U^{4+}, Zr^{4+}, Hf^{4+}, Ti^{4+}, Nb^{5+}, and Ta^{5+}. This is consistent with previous studies that have found high concentrations of many of these elements in cassiterite (Möller and Dulski, 1983; Möller et al., 1988; Plimer et al., 1991; Murciego et al., 1997). Most of these elements are also present in appreciable quantities in the 6 Gejiu cassiterite samples examined here, although there are some significant compositional differences between each of these cassiterite samples, which may provide information on the composition of the source fluids and on cassiterite precipitation processes.

Quadrivalent elements such as Zr, Hf, Ti, U^{4+} and W^{4+} can substitute directly for Sn^{4+} in cassiterite without any additional charge balance considerations. Zirconium and Hf are considered to be geochemical “twins”, and therefore these elements maintain a relatively constant near chondritic Zr/Hf ratio of 35 to 40 in most geological systems (Hoskin and Schaltegger, 2003). Rare cases of significant deviation of this ratio occur in some hydrothermal and highly differentiated igneous rocks, but the causative mechanism for fractionation are not yet well understood. Processes that have been proposed to fractionate Zr and Hf include metasomatism (e.g., Dupuy et al., 1992; Rudnick et al., 1993; Bau, 1996), crystal fractionation involving accessory phases such as zircon (e.g., Linnen, 1998; Claiborne et al., 2006), or hydrothermal alteration (e.g., Rubin et al., 1993; Jiang et al., 2005). Zr/Hf ratios of Gejiu cassiterites exhibit significant variation from greisen-hosted cassiterite with Zr/Hf ratios of about 12.5, to tin granite cassiterite (~16.7), skarn/semi-oxidized/oxidized ore cassiterite (~25), and vein ore cassiterite (67) (Fig. 7B). Tourmaline and fluorite are abundant in vein ores (see Cheng, 2012), indicating that the mineralizing fluids were rich in B and F. Such fluid compositions have been proposed to preferentially mobilize Zr relative to Hf (Rubin et al., 1993; Jiang et al., 2005), which may explain the higher Zr/Hf in vein cassiterite compared to that of other samples. The relatively low Zr/Hf ratio in the tin granite and greisen ores may be complementary to the high Zr/Hf fluid that precipitated the vein ore cassiterite.

Cassiterite Ti/Zr ratios vary by over an order of magnitude in all of the samples, which reflects intra-grain elemental variations, as also revealed by element maps. The cause of such large variations is poorly understood, but is likely a product of localized elemental fractionation during grain growth. Nevertheless, we also observe an overall decrease in Ti/Zr ratio with distance from the host intrusion (Fig. 7C). We note that there are no Ti- or Zr–rich minerals associated with any of the ore mineral assemblages examined here (see above), so we discount fractionation of Ti/Zr by co-crystallizing hydrothermal mineral phases. The crystallizing granite is regarded as the source of mineralizing fluids for all ore environments (Appendix 1-1; Cheng, 2012), so the decrease in Ti/Zr ratio can be considered to reflect progressive depletion of Ti relative to Zr from the fluid as it migrates and evolved away from the intrusion. This trend would be consistent with results of some studies that show higher solubility of Zr in fluids compared to Ti (e.g., Kessel et al. 2005). In this case, Ti/Zr ratio of cassiterite has potential to be used to vector towards the causative intrusion in Sn mineralized systems, provided that the large intra-grain and intra-sample variations are accounted for.

As with Zr-Hf systematics, Nb and Ta have similar ionic charge and ionic radii, and thus also display very similar geochemical behavior, leading to relativity uniform Nb/Ta values in terrestrial reservoirs of between 10 and 20 (Münker et al., 2003). The Nb/Ta ratios of cassiterite samples examined here range from <1 up to ~400 (Appendix 3). Variations of Nb/Ta in tin granite, greisen ore, and skarn ore cassiterites are approximately three times greater than those of cassiterite from the other 3 ore environments. Preferred partitioning of one element over the other by cassiterite cannot simply explain the large range of Nb/Ta values in all samples; rather we appeal to more complex processes, such as elemental fractionation during mineral growth due to localized fluid disequilibria and/or sluggish element diffusion (e.g., Foley et al., 2000; Pieczka, 2010; Cherniak, 2015). Such mechanisms would also be consistent with the >4 orders of magnitude concentration range of these elements. A thorough examination of these variations is beyond the scope of this paper, but is worthy of further investigation.

The geochemical behavior of V, Ga, and Sc in hydrothermal fluids is poorly understood, particularly in relation to partitioning between fluid and cassiterite. In the Gejiu cassiterite samples, we recognize a clear positive correlation between V and Sc, and between Ga and Fe (Fig. 8E, F). Under geological conditions Sc only has one valence state (3+), so the positive V-Sc correlation in cassiterite leads to speculation that V substitutes in the 5+ valence state, allowing a charge-balanced coupled substitution of $Sc^{3+} + V^{5+} = 2Sn^{4+}$. Both Fe and Ga are likely present in cassiterite as trivalent cations (see discussion below regarding trivalent Fe), so their close correlation may be due to their very similar ionic radii (Fig. 1).

Perhaps the simplest form of charge balance for many elements in cassiterite is the coupled substitution of a trivalent cation and a pentavalent cation for two Sn^{4+} cations, as we propose for Sc and V above. If such a mechanism dominates for cassiterite, we should see a 1:1 balance between total trivalent (Al, Sc, Fe, Ga, Sb) and total pentavelent (V, Nb, Ta) cations (note, W and U are regarded to be quadrilavent, as discussed below). However, we observe a significant excess in trivalent cations in almost all cases (Fig. 8D), which means there needs to be an additional mechanism to incorporate these trivalent cations (mostly Fe^{3+}). We favour a coupled Fe^{3+} plus H^{+} substitution of Sn^{4+}, as previously proposed (Möller et al., 1988; Tindle and Breaks, 1998; Pieczka et al., 2007).

Monitors of fluid redox conditions

Both the element maps and trace element spot data reveal distinct compositional zones that are either W+U (+Sb) rich, and Fe poor, or vice versa. These compositional domains cut across the primary oscillatory zoning (Fig. 6) and so are considered to postdate primary cassiterite growth. Nonetheless, aspects of the primary oscillatory zoning are preserved throughout these domains. As far as we are aware, these compositional features have not previously been reported for cassiterite. These features, together with the sharp boundary between domains and preservation of the original external crystal morphology, are all characteristics of coupled dissolution-reprecipitation textures documented in natural and experimentally re-equilibrated minerals (Putnis, 2002; Parsons and Lee, 2005; Harlov et al., 2011; Ague and Axler, 2016). Therefore, we interpret these features to represent domains of cassiterite that underwent partial dissolution-reprecipitation via hydrothermal fluids after primary cassiterite growth. Coupled dissolution-reprecipitation involves microscale mineral replacement via a fluid phase (Putnis 2002), which can only progress if fluid interconnection is maintained via micro- to nano-scale porosity within the mineral. Evidence of fluid connectivity is usually preserved as pores or fluid inclusions in the replaced mineral domains (Putnis, 2002). Our cassiterite grains are devoid of remnants of porosity (i.e., no fluid inclusions or pores; Fig. 6), indicating that the fluid pores/channels are too fine (nano-scale) to observe with our methods or that the porosity was transient, with pore space being erased via local annealing once recrystallization had proceeded. Harlov et al. (2011) and Ague and Axler (2016) appealed to similar processes to explain the lack of preserved porosity in dissolution-repreciation zones of monazite and garnet, respectively.

Dissolution-reprecipitation processes are thought to be driven by changing the physical conditions or chemical environment (fluid composition) of a mineral, so our trace element compositional data and U-Pb dating for these domains may be able to inform us about the physical and/or chemical conditions of the altering fluids and timing of the alteration. We argue that the compositional differences between the cassiterite domains are not directly reflecting the varying trace element composition of the fluid phase, as: 1) there is no observable variation in most compatible elements (e.g., Ti, Zr, Hf, Nb, Ta) between domains, and; 2) fluids of highly contrasting elemental composition would be required to explain the orders of magnitude variation in concentrations of W, U, and Fe between domains. We see no other evidence for such extreme fluid compositions from our samples or from previous studies.

A key observation is that all of the elements that define the dissolution-reprecipitation domains can occur in more than one redox state under geological conditions. Tungsten and U are expected to occur as either 4+ or 6+ (and possibly 5+) ions, Fe can be divalent or trivalent, and Sb may be either trivalent or pentavalent. As valence state directly impacts the compatibility of an element in cassiterite (Fig. 1), we interpret the distinct concentration differences of these elements between domains to reflect redox-driven chemical modification of cassiterite by reaction with hydrothermal fluid. We interpret the high W+U (+Sb), low Fe oscillatory-zoned cassiterite (Figs. 6 and 8) to represent the primary (original) cassiterite formed under relatively reduced conditions where Sn^{2+} can be transported in acidic fluids (see Heinrich, 1990). Under these conditions W and U are primarily quadrivalent and, hence, are compatible in cassiterite, whereas divalent Fe is incompatible (Fig. 1). The dissolution-reprecipitation domains have high Fe and low W and U, which we interpret to result from mineral reaction with relatively oxidising fluid in which most Fe becomes trivalent and compatible, and U and W are (at least partly) in the 5+ or 6+ state, and hence incompatible in cassiterite (Fig. 1). The higher Sb concentration in the primary zones may indicate that Sb^{3+} is more compatible in cassiterite than Sb^{5+}. Mineral reaction is interpreted to proceed via cation exchange wherein every 4 atoms of Fe^{3+} (from the fluid) substitute into cassiterite for 3 atoms of W^{4+} or U^{4+}, plus a site vacancy. In their oxidized states, W and U are fluid mobile and are transported out of the cassiterite. Notwithstanding the appreciable range of Fe, W and U contents of these zones, this proposed substitution mechanism is broadly consistent with the concentrations of observed for U and W, and Fe in the respective primary and secondary zones (Fig. 6). Support for such a process can be seen in the continuation of oscillatory zoning across the two domains; for example, µm-sized zones of high W and U in the primary cassiterite directly extend across the domain boundary to zones with high Fe contents in the dissolution-reprecipitation zone. We are unaware of any other report where the trace of primary oscillatory zoning is preserved through the process of dissolution-reprecipitation. Elements that are not redox sensitive and are not typically fluid mobile (Ti, Zr, Hf, Nb, Ta) remain unaffected by this process, and so have concentration zoning patterns that are continuous across the domain boundaries.

In the present case, we can only speculate that the origin of the secondary oxidized fluid may be due to influx of meteoric fluid or other external fluids. Nonetheless, these results do indicate that combining textural studies of cassiterite zoning with the distribution and concentration of redox sensitive elements, such as W, U, Fe, and Sb, can be a powerful tool for evaluating the redox conditions of mineralizing fluids and mineral precipitation processes. This approach may be especially useful for understanding Sn mineralization systems, as changes in redox, and fluid mixing or reaction are considered to be among the most important drivers of Sn ore formation (Heinrich, 1990). We expect that this approach would be applicable to Sn ore fields worldwide, and may also be applicable to other metal oxide minerals, such as rutile and wolframite.

In situ cassiterite U-Pb geochronology

Precise and accurate age determination of mineral deposits is essential for proper understanding of ore genesis. Researchers have shown the potential for U-Pb dating of cassiterite using a variety of analytical techniques (Gulson and Jones, 1992; Yuan et al., 2008; Blevin and Norman, 2010; Zhang et al., 2015; Guo et al., 2018). Here we acquired ^{206}Pb-^{238}U ages of between 77.2 ± 0.5 Ma to 83.6 ± 1.3 Ma for the 6 cassiterite samples from Gejiu district by LA-ICP-MS. These ages are consistent with ages determined by other dating methods in this area, including 13 ^{40}Ar–^{39}Ar ages of hydrothermal mica that range from 77.4 ± 0.6 Ma to 95.3 ± 0.7 Ma, 2 Re-Os molybdenite ages of 83.4 ± 2.1 Ma and 84.2 ±7.3 Ma, and 15 U-Pb zircon ages or igneous rocks that range from 77.4 ± 2.5 Ma to 85.8 ± 0.6 Ma (Cheng, 2012). The consistency of these dating results demonstrates the utility of LA-ICP-MS U–Pb dating of cassiterite for directly determining the age of Sn deposits. Of note, the ages obtained on the dissolution-reprecipitation domains in the tin granite, skarn, and greisen samples are within error of the primary cassiterite ages, indicating hydrothermal alteration occurred soon after (i.e. within 3 m.y.) primary Sn mineralization.

Tin polymetallic ores in the Gejiu district have long been considered to be of hydrothermal origin with a genetic relationship to Cretaceous granites (e.g., 308 Geological Party, 1984). However, based on different dating results, including mica ^{40}Ar-^{39}Ar ages ranging from 83.2 ± 2.1 to 205.1 ± 4.4 Ma (Qin et al., 2006) and cassiterite K-Ar ages from 43.5 ± 0.9 Ma to 186.0 ± 3.7 Ma (Li et al., 2009), it has been argued that Sn polymetallic ores in Gejiu district may be of syngenetic origin (e.g., Qin et al., 2006). Our new U–Pb ages for cassiterite all fall between 78–84 Ma in age, which is in excellent agreement with the Late Cretaceous magmatic emplacement ages. This temporal link between the granite and mineralization supplements evidence obtained from geologic characteristics, fluid inclusions, isotopes, and mineral chemistry (Cheng, 2012) supporting an intrusion-related origin for hydrothermal alteration and sulfide and tin mineralization in the Gejiu district

IMPLICATIONS

A combination of microtextural imaging by CL, LA-ICP-MS trace-element analysis and U-Pb dating provide new insights into ore genesis and Sn mineralization in the world-class Gejiu tin district, as follows:

(1) Cassiterite grains from tin granite, greisen, and skarn ores are generally large, and characterized by euhedral oscillatory growth zones, but do feature domains rich in W and U, and depleted in Fe, that irregularly cross-cut the primary growth zones. Cassiterite from semi-oxidized ores, stratiform oxidized ores and distal veins are typically smaller, anhedral crystals with less regular zoning patterns.

(2) A range of trivalent, quadrivalent, and pentavalent trace elements are present in appreciable, but variable, amounts. The most abundant elements are Fe, Ti, and W, and the concentrations of Nb and Ta exhibit the largest variations amongst all the elements. Zr/Hf ratios of the 6 samples exhibit vary from greisen-hosted cassiterite to vein-hosted cassiterite, which is attributed to different F and B activities in the different environments. Ti/Zr ratio also decreases with distance from the host granite intrusion.

(3) The irregular W+U depleted, Fe-rich domains in the tin granite, greisen, and skarn cassiterites represents zones of dissolution-reprecipitation due to interaction of relatively oxidised hydrothermal fluids. Examination of redox sensitive elements in cassiterite and other hydrothermal metal oxides from other ore fields may provide important insights into oxygen fugacity controls on ore mineral formation and alteration.

(4) U-Pb geochronology by LA-ICP-MS reveals cassiterite ages in the range ~77 Ma to ~83 Ma, which is consistent with previous findings that the Gejiu tin deposits are hydrothermal in origin and temporally, spatially, and genetically associated with the emplacement of the Gejiu granitic complex. These results suggest that U-Pb analysis of cassiterite by LA-ICP-MS may be a reliable tool for directly constraining the timing of tin ore formation, with the caveat that well characterized cassiterite age standards are required for the accuracy of the method to be rigorously assessed.

ACKNOWLEDGMENTS

We thank the handling editor (Dr. Sarah Penniston-Dorland), Prof. David Lentz and one anonymous reviewers for their comments on our manuscript, and appreciate the assistance of Guopei Mo, Xiang Tong, Junde Wu and other colleagues from Yunnan Tin Group, and Xiaolong Li and Juan Zhang from China University of Geosciences (Beijing) during our fieldwork. This study was supported by the National Science Foundation of China (40930419), Special Research Funding for the Public Benefits Sponsored by MLR (200911007-12), Research Program of Yunnan Tin Group (2010-04A), and Geological Investigation Program by CGS (1212011120994). Kemp and Spandler acknowledge support from Australian Research Council fellowships (FT100100059 and FT120100198).

REFERENCES CITED

308 Geological Party (1984) Geology of tin deposit in Gejiu area. Beijing, Metallurgical Industry Publishing House, p. 236.

Ague, J.J. and Axler, J.A. (2016) Interface coupled dissolution-reprecipitation in garnet from subducted granulites and ultrahigh-pressure rocks revealed by phosphorous, sodium, and titanium zonation. American Mineralogist, 101, 1696-1699.

Bau, M. (1996) Controls on the fractionation of isovalent trace elements in magmatic and aqueous systems: evidence from Y/Ho, Zr/Hf, and lanthanide tetrad effect. Contribution to Mineralogy and Petrology, 123, 323–333.

Blevin, P.L. and Norman, M. (2010) Cassiterite-The Zircon of mineral systems? A scoping study, p. 399–400. In Geological Society of Australia, 2010 Australian Earth Sciences Convention (AESC) 2010, Earth systems: change, sustainability, vulnerability. Abstract No 98 of the 20th Australian Geological Convention, National Convention Centre, Canberra, Australian Capital Territory. July 4-8.

Chen, W., and Simonetti, A. (2012) In-situ determination of major and trace elements in calcite and apatite, and U–Pb ages of apatite from the Oka carbonatite complex: Insights into a complex crystallization history. Chemical Geology, 353, 151-172.

Cheng, Y.B., and Mao, J.W. (2010) Age and geochemistry of granites in Gejiu area, Yunnan province, SW China: constraints on their petrogenesis and corresponding tectonic setting. Lithos, 120, 258–276.

Cheng, Y.B. (2012) Spatial-temperal evolution of the magmatism and mineralization in the Gejiu supergiant Sn polymetallic district and insights into several key problems. PhD thesis, China University of Geosciences (Beijing) (in Chinese with English abstract).

Cheng, Y., Spandler, C., Mao, J., and Rusk, B.G. (2012) Granite, gabbro and mafic microgranular enclaves in the Gejiu area, Yunnan Province, China: a case of two-stage mixing of crust-and mantle-derived magmas. Contributions to Mineralogy and Petrology, 164, 659-676.

Cheng, Y., Mao, J., Chang, Z., and Pirajno, F. (2013) The origin of the world class tin-polymetallic deposits in the Gejiu district, SW China: constraints from metal zoning characteristics and ^{40}Ar-^{39}Ar geochronology. Ore Geology Reviews, 53, 50-62.

Cheng, Y., Mao, J., Zhu, X., and Wang, Y. (2015) Iron isotope fractionation during supergene weathering process and its application to constrain ore genesis in Gaosong deposit, Gejiu district, SW China. Gondwana Research, 27, 1283-1291.

Cheng, Y., Spandler, C., Chang, Z., and Clarke, G. (2018) Volcanic-plutonic connections and metal fertility of highly evolved magma systems: a case study from the Herberton Sn-W-Mo Mineral Field, Queensland, Australia. Earth and Planetary Science Letters, 486, 84-93.

Cherniak, D.J. (2015) Nb and Ta diffusion in titanite. Chemical Geology, 413, 44-50.

Chew, D.M., Petrus, J.A. and Kamber, B.S. (2014) U–Pb LA–ICPMS dating using accessory mineral standards with variable common Pb. Chemical Geology, 363, 185–199.

Claiborne, L.L., Miller, C.F., Walker, B.A., Wooden, J.L., Mazdab, F.K. and Bea, F. (2006) Tracking magmatic processes through Zr/Hf ratios in rocks and Hf and Ti zoning in zircons: An example from the Spirit Mountain batholith, Nevada. Mineralogical Magazine, 70, 517–543.

Dupuy, C., Liotard, J.M. and Dostal, J. (1992) Zr/Hf fractionation in intraplate basaltic rocks: carbonate metasomatism in the mantle source. Geochimica et Cosmochimica Acta, 5, 2411-2423.

Farmer, C.B., Searl, A. and Halls, C. (1991) Cathodoluminescence and growth of cassiterite in the composite lodes at South Crofty Mine, Cornwall, England. Mineralogical Magazine, 55, 447-458.

Foley, S.F., Barth, M.G., and Jenner, G.A. (2000) Rutile/melt partition coefficients for trace elements and an assessment of the influence of rutile on the trace element characteristics of subduction zone magmas. Geochimica et Cosmochimica Acta, 64, 933–938.

Giuliani, G. (1987) La cassiterite zonee du gisement de Sokhret Allal (Granite des Zaer, Maroc Central): composition chimique et phases fluides associees. Mineralium Deposita, 22, 253-261.

Götze, J. and Kempe, U. (2008) A comparison of optical microscope- and scanning electron microscope-based cathodoluminescence (CL) imaging and spectroscopy applied to geosciences. Mineralogical Magazine, 72, 909-924.

Gulson, B.L., and Jones, M.T. (1992) Cassiterite: Potential for direct dating of mineral deposits and a precise age for the Bushveld Complex granites. Geology, 20, 355-358.

Guo, J., Zhang, R.Q., Sun, W.D., Ling, M.X., Hu, Y.B., Wu, K., Luo, M., and Zhang, L.C. (2018) Genesis of tin-dominant polymetallic deposits in the Dachang district, South China: Insights from cassiterite U–Pb ages and trace element compositions. Ore Geology Reviews, 95, 863-879.

Hammerli, J., Rusk, B., Spandler, C., Emsbo, P., and Oliver, N.H.S. (2013) In situ quantification of Br and Cl in minerals and fluid inclusions by LA-ICP-MS: A powerful tool to identify fluid sources. Chemical Geology, 337–338, 75-87.

Harlov, D.E., Wirth, R., and Hetherington, C.J. (2011) Fluid-mediated partial alteration in monazite: the role of coupled dissolution–reprecipitation in element redistribution and mass transfer. Contribution to Mineralogy and Petrology, 162, 329–348.

Heinrich, C.A. (1990) The chemistry of tin (-tungsten) ore deposition. Economic Geology, 85, 529-550.

Heinrich, C.A. (1995) Geochemical evolution and hydrothermal mineral deposition in Sn (– W - base metal) and other granite-related ore systems: Some conclusions from Australian examples. In Magmas. Fluids and Ore Deposits (ed. Thompson J.F.H.). Geological Association of Canada Short Course Series, 23, 203-220.

Hoskin, P.W.O. and Schaltegger, U. (2003) The composition of zircon and igneous and metamorphic petrogenesis. p. 27-62. In: Zircon (ed. Hanchar J.M. and Hoskin P.W.O.). Reviews in Mineralogy and Geochemistry, 53, Mineralogical

Society of America, Washington, D.C.

Jiang, S.Y., Wang, R.C., Xu, X.S. and Zhao, K.D. (2005) Mobility of high field strength elements (HFSE) in magmatic-, metamorphic-, and submarine-hydrothermal systems. Physics and Chemistry of the Earth, 30, 1020–1029.

Kessel, R., Ulmer, P., Pettke, T., Schmidt, M.W. and Thompson, A.B. (2005) The water-basalt system at 4 to 6 GPa: Phase relations and second critical endpoint in a K-free eclogite at 700 to 1400 °C. Earth and Planetary Science Letter, 237, 873–892.

Lehmann, B. (1990) Metallogeny of tin. Springer, Berlin.

Linnen, R.L. (1998) The solubility of Nb–Ta–Zr–Hf–W in granitic melt with Li and Li+F: constraints for mineralization in rare metal granite and pegmatite. Economic Geology, 93, 1013–1025.

Ludwig, K.R. (2003) Isoplot/Ex Version 3.00: a Geochronological Toolkit for Microsoft Excel. Berkeley Geochronology Center, Berkeley, C.A.

Mao, J.W., Cheng, Y.B, Guo, C.L, Yang, Z.X. and Zhao, H.J. (2008) Gejiu tin polymetallic ore-field: deposit model and discussion. Acta Geologica Sinica, 81, 1456-1468 (in Chinese with English abstract).

Möller, P. and Dulski, P. (1983) Fractionation of Zr and Hf in cassiterite. Chemical Geology, 40, 1-12.

Möller, P., Dulski, P., Szacki, W., Malow, G., and Riedel, E. (1988) Substitution of tin in cassiterite by tantalum, niobium, tungsten, iron and manganese. Geochimica et

Cosmochimica Acta, 52, 1497-1503.

Moore, F., and Howie, R.A. (1979) Geochemistry of some Cornubian cassiterites. Mineral. Deposita, 14, 103-107.

Münker, C., Pfänder, J.A., Weyer, S., Büchl, A., Kleine, T., Mezger, K. (2003) Evolution of planetary cores and the Earth - Moon system from Nb/Ta systematics. Science, 301, 84-87.

Murciego, A., Sanchez, A.G., Dusausoy, Y, Pozas, J.M.M., and Ruck, R. (1997) Geochemistry and EPR of cassiterites from the Iberian Hercynian Massif. Mineralogical Magazine, 61, 357-365.

Parsons, I., and Lee, M.R. 2005, Minerals are not just chemical compounds. Canadian Mineralogist, v. 43, p. 1959–1992.

Pieczka, A., Goebiowska, B. and Parafiniuk, J. (2007) Geochemistry and origin of the cassiterite from Redziny, Lower Silesia, Poland. Mineralogia Polonica, 38, 219-229.

Pieczka, A. (2010) Primary Nb-Ta minerals in the Szklary pegmatite, Poland: New insights into controls of crystal chemistry and crystallization sequences. American Mineralogist, 95, 1478-1492.

Plimer, I.R., Lu, J., and Kleeman, J.D. (1991) Trace and rare earth elements in cassiterite - sources of components for the tin deposits of the Mole Granite, Australia. Mineralium Deposita, 26, 267-274.

Putnis, A. (2002) Mineral replacement reactions: from macroscopic observations to microscopic mechanisms. Mineralogical Magazine, 66, 689-708.

Qin, D.X., Li, Y.S. and Tan, S.C. (2006) Metallogenic ages of Gejiu tin deposit in Yunnan Province. Chinese Journal of Geology, 41, 122-132 (in Chinese with English abstract).

Rubin, J.N., Henry, C.D. and Price, J.G. (1993) The mobility of zirconium and other immobile elements during hydrothermal alteration. Chemical Geology, 110, 29–47.

Rudnick, R.L., McDonough, W.F. and Chappell, B.W. (1993) Carbonatite metasomatism in the northern Tanzanian mantle: petrographic and geochemical characteristics. Earth and Planetary Science Letters, 114, 463–475.

Rusk, B., and Reed, M. (2002) Scanning electron microscope-cathodoluminescence of quartz reveals complex growth histories in veins from the Butte porphyry copper deposit, Montana. Geology, 30, 727–730.

Rusk, B., Lowers, H. and Reed, M. (2008) Trace elements in hydrothermal quartz: relationships to cathodoluminescent textures and insights into hydrothermal processes. Geology, 36, 547–550.

Schneider, H.J., Dulski, P., Luck, J., Moeller, P. and Villalpando, A. (1978) Correlation of trace element distribution in cassiterites and geotectonic position of their deposits in Bolivia. Mineralium Deposita, 13, 119-22.

Shannon, R.D. (1976) Revised effective ionic radii and systematic studies of interatomic distances in halides and chalcogenides. Acta Crystallographica Section A, 32, 751-767.

Spandler, C., Pettke, T. and Rubatto, D. (2011) Internal and external fluid sources for eclogite-facies veins in the Monviso meta-ophiolite, Western Alps: implications for fluid flow in subduction zones. Journal of Petrology, 52, 1207-1236.

Stacey, J.S. and Kramers, J.D. (1975) Approximation of terrestrial lead isotope evolution by a two-stage model. Earth and Planetary Science Letter, 26, 207–221.

Tindle, A.G. and Breaks, F.W. (1998) Oxide minerals of the Separation Rapids rare-element granitic pegmatite group, northwestern Ontario. Canadian Mineralogist, 36, 609–635.

Tucker, R.T., Roberts, E.M., Hu, Y., Kemp, A.I.S., and Salisbury S.W. (2013) Detrital zircon age constraints for the Winton Formation, Queensland: contextualizing Australia's Late Cretaceous dinosaur faunas. Gondwana Research, 24, 767–779.

Van Achterbergh, E., Ryan, C., Jackson, S.E. and Griffin, W.L. (2001) Appendix 3 data reduction software for LA-ICP-MS. In Laser-Ablation-ICPMS in the Earth Sciences. Mineralogical Association of Canada, Short Course (ed. Sylvester, P.), p. 239-243.

Yuan, S.D., Peng, J.T., Hu, R.Z., Li, H.M., Shen, N.P. and Zhang, D.L. (2008) A precise U–Pb age on cassiterite from the Xianghualing tin–polymetallic deposit (Hunan, South China). Mineralium Deposita, 43, 375–382.

Zhang, R.Q., Lu, J.J., Wang, R.C., Yang, P., Zhu, J.C., Yao, Y., Gao, J.F., Li, C., Lei, Z.H., Zhang, W.L., and Guo, W.M. (2015) Constraints of in-situ zircon and cassiterite U–Pb, molybdenite Re–Os, and muscovite ^{40}Ar–^{39}Ar ages on multiple generations of granitic magmatism and related W–Sn mineralization in the

Wangxianling area, Nanling Range, South China. Ore Geology Reviews, 65, 1021-1042.

Zhuang, Y.Q., Wang, R.Z. and Yang, S.P. (1996) Tin-copper polymetallic deposits in Gejiu district. Earthquake Publishing House, Beijing (in Chinese).

Figure Captions

Fig. 1. Plot of ionic charge against ionic radius (6-fold coordination, from Shannon, 1976) for elements investigated in this study.

Fig. 2. Geological map of the Gejiu ore district and cross section of the mining district (Modified from Mao et al., 2008).

Fig. 3. Six types of representative mineralization environments of the Gejiu ore district. a. tin granite; b. greisen ore; c. skarn ore; d. semioxidized ore; e. oxidized ore; f. vein ore.

Fig. 4. Optical microscope images under plane polarized light (a), and crossed polarized light (b) of cassiterite from greisen sample A0374-7, showing the intergrowth of K-feldspar, quartz, and cassiterite. Definitions of mineral abbreviations: Qtz-Quartz; Cst-Cassiterite; Kfs-K-feldspar.

Fig. 5. Selected cathodoluminescence (CL) images of the six types of cassitierite samples. Note that the grain size and zoning features are different between the proximal cassiterite samples (tin granite, greisen ore and skarn ore) and the distal samples (semi-oxidized, oxidized and vein ore cassiterite).

Fig. 6. Coupled BSE and CL images, and EPMA and LA-ICP-MS multiple element

mapping results of cassiterite from greisen sample (A0374-7). A and B: BSE and CL images of the targeted cassiterite grain; C-F: EPMA mapping results of W, Fe, Nb and Ti in the cassiterite grain; G: analytical spots in the cassiterite grain under optical microscope; H-N: LA-ICP-MS mapping results of W, U, Fe, Sc, Ti, Nb, and Ta in the cassiterite grain. The white rectangle in Figure 6b represents the whole area of the Figure 6c-f.

Fig. 7. Niobium versus Ta, Zr versus Hf, and Ti/Zr against sample location for the Gejiu cassiterite samples. Note the positive correlations between Nb and Ta, Zr and Hf in all 6 samples, and the broad decrease of Ti/Zr ratios with distance from the causative intrusion.

Fig. 8. Selected scatterplots of trace element in the cassiterite samples. Samples proximal to the intrusion (tin granite, skarn, and greisen) are displayed with colored symbols and distal samples (oxidized, semi-oxidized, and vein) are displayed with grey and black symbols.

Fig. 9. LA-ICP-MS U–Pb ages for various cassiterite samples and domains. U-Pb isotopes on both U enriched and U depleted zones were analyzed to evaluate the cassiterite U-Pb dating reliability in domains of different U content. The red color refers to the analyses in high U zones, while blue color represents the analyses in low U zones. It is worth noting that the data presented in above diagrams are

representative of analyses that are concordant or near concordant

Table/Appendix Captions

Table 1. Brief description of the six samples of this study.

Appendix 1. Extra figures show the field locations and relationship of the examined samples of this study (Appendix 1-1).

Appendix 2 Down-hole Pb/U fractionation between zircon, cassiterite and NIST glass by LA-ICP-MS (Appendix 2-1), the LA-ICP-MS spectra of signal intensity of common Pb of the analyzed cassiterite samples (Appendix 2-2), and analytical result (Appendix 2-3) and the Concordia diagram (Appendix 2-4) of LA-ICP-MS cassiterite U-Pb dating on cassiterite samples hosted by a Carboniferous tin granite of the Herberton area, north Queensland, Australia.

Appendix 3. Trace element compositions of the six cassiterite samples.

Appendix 4. Uranium-Pb dating results for the six Gejiu cassiterite samples analyzed by LA-ICP-MS.

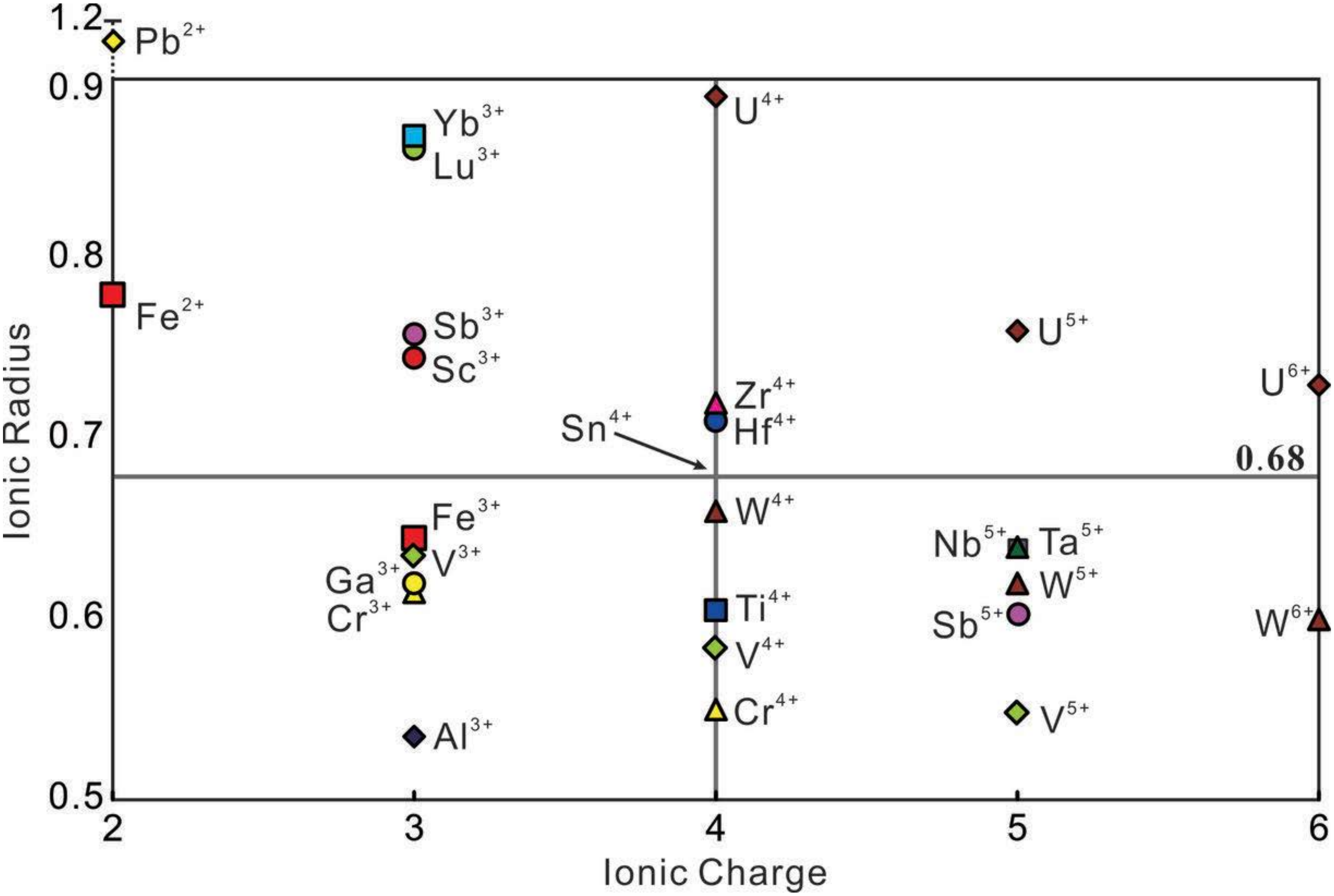
1.2
0.9
0.8
0.7
0.6
0.5
Ionic Radius
2
3
4
5
6
Ionic Charge
Pb^{2+}
Fe^{2+}
Yb^{3+}
Lu^{3+}
Sb^{3+}
Sc^{3+}
Fe^{3+}
V^{3+}
Ga^{3+}
Cr^{3+}
Al^{3+}
U^{4+}
Zr^{4+}
Hf^{4+}
Sn^{4+}
W^{4+}
Ti^{4+}
V^{4+}
Cr^{4+}
U^{5+}
Nb^{5+}
Ta^{5+}
W^{5+}
Sb^{5+}
V^{5+}
U^{6+}
W^{6+}
0.68

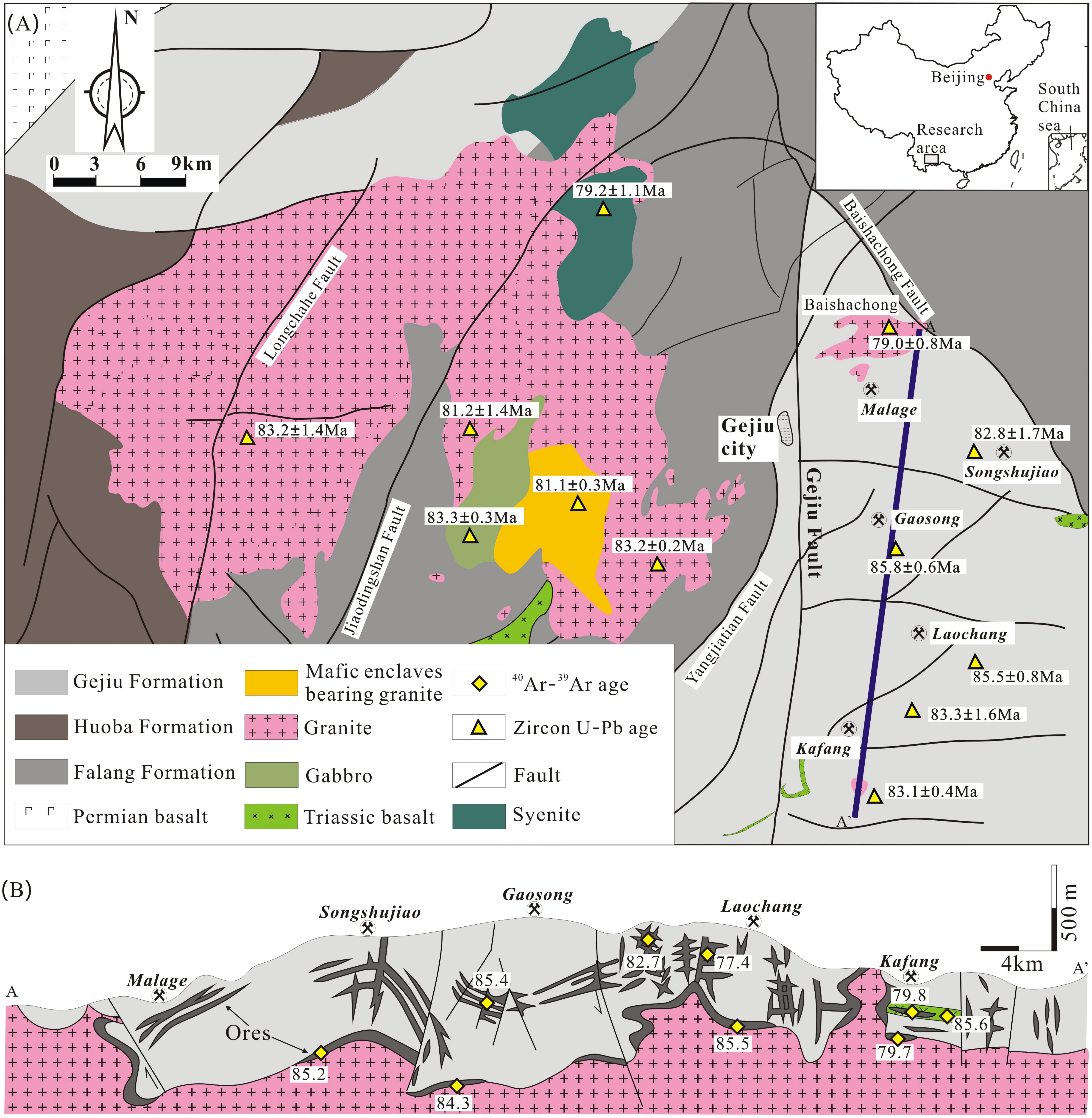
(A)
N
0 3 6 9km
Beijing
South China sea
Research area
79.2±1.1Ma
Longchahe Fault
Baishachong Fault
Baishachong
A
79.0±0.8Ma
Malage
81.2±1.4Ma
83.2±1.4Ma
Gejiu city
82.8±1.7Ma
Songshujiao
81.1±0.3Ma
Gejiu Fault
83.3±0.3Ma
Gaosong
Jiaodingshan Fault
83.2±0.2Ma
85.8±0.6Ma
Yangjiatian Fault
Laochang
85.5±0.8Ma
83.3±1.6Ma
Kafang
83.1±0.4Ma
A'
Gejiu Formation
Huoba Formation
Falang Formation
Permian basalt
Mafic enclaves bearing granite
Granite
Gabbro
Triassic basalt
^{40}Ar-^{39}Ar age
Zircon U-Pb age
Fault
Syenite
(B)
Gaosong
Songshujiao
Laochang
500 m
4km
A
Malage
82.7
77.4
Kafang
A'
85.4
79.8
Ores
85.6
85.5
85.2
79.7
84.3


a
Cassiterite
Granite
b
Quartz
Muscovite
Tourmaline
Greisen Ore
c
Quartz
Pyroxene
Skarn Ore
Garnet
Mineralium Deposita
SGA
Society for Geology
d
Top
Oxidized ore
Semi-oxidized
Oxidized ore
Bottom
e
Wall rock: Carbonate
Oxidized ore
f
Tourmaline
Vein ore
Carbonate

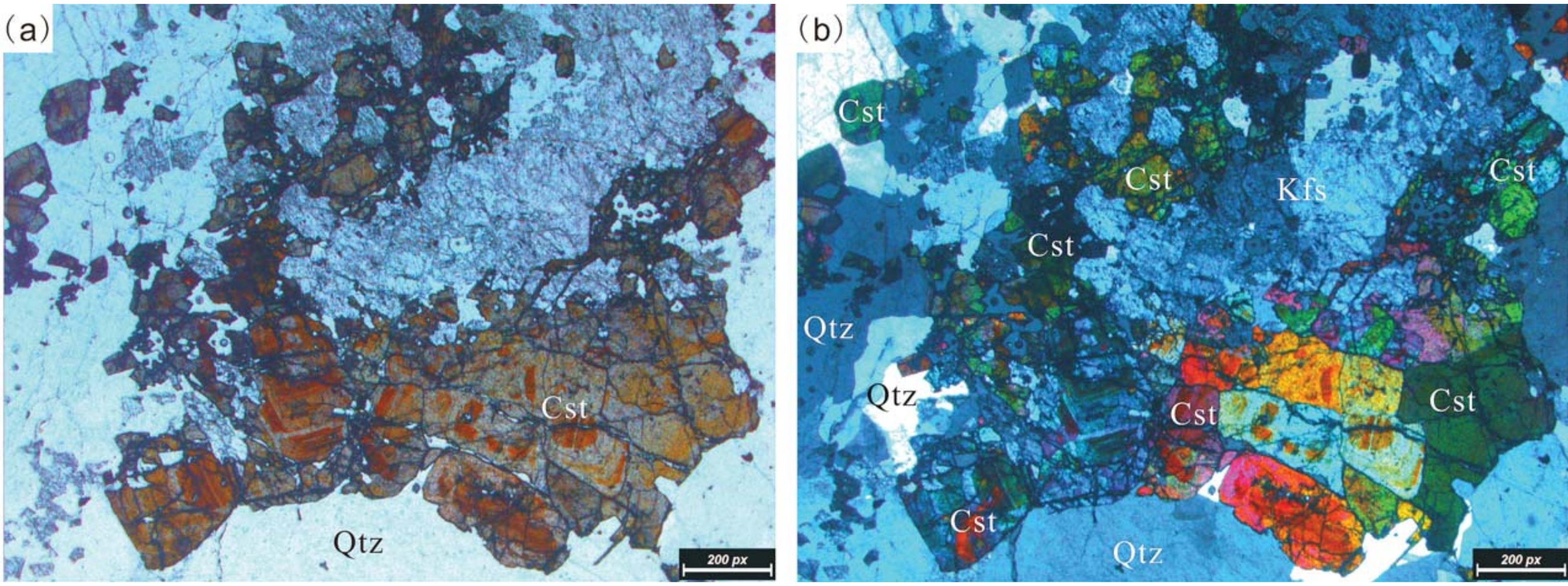
(a)
Cst
Qtz
200 px
(b)
Cst
Cst
Kfs
Cst
Cst
Qtz
Qtz
Cst
Cst
Cst
Qtz
200 px


Tin granite
300 μm
Greisen ore
500 μm
Skarn ore
200 μm
Semioxidized ore
200 μm
Oxidized ore
200 μm
Vein ore
500 μm


A
B
100μm
C
W
0
520 um
D
Fe
0
520 um
E
Nb
0
520 um
F
Ti
0
520 um
G
H
W(ppm)
I
U(ppm)
J
Fe (ppm)
K
Sc (ppm)
L
Ti (ppm)
M
Nb (ppm)
N
Ta (ppm)


(A)
Ta (ppm)
1000
100
10
1
0.1
0.01
0.001
Nb (ppm)
0.1
1
10
100
1000
Semi-oxidized Ore
Oxidized Ore
Vein ore
(B)
Hf (ppm)
8
7
6
5
4
3
2
1
0
Zr (ppm)
0
100
200
300
Zr/Hf=~12.5
Zr/Hf=~25
Zr/Hf=~66.5
Tin granite
Greisen Ore
Skarn Ore
(C)
Ti/Zr
10000
1000
100
10
1
0.1
Proximal samples
Distal samples
125
93
61
27
43
3
Tin granite
Greisen Ore
Skarn Ore
Semi-oxidized Ore
Oxidized Ore
Vein Ore
Relative distance form granite

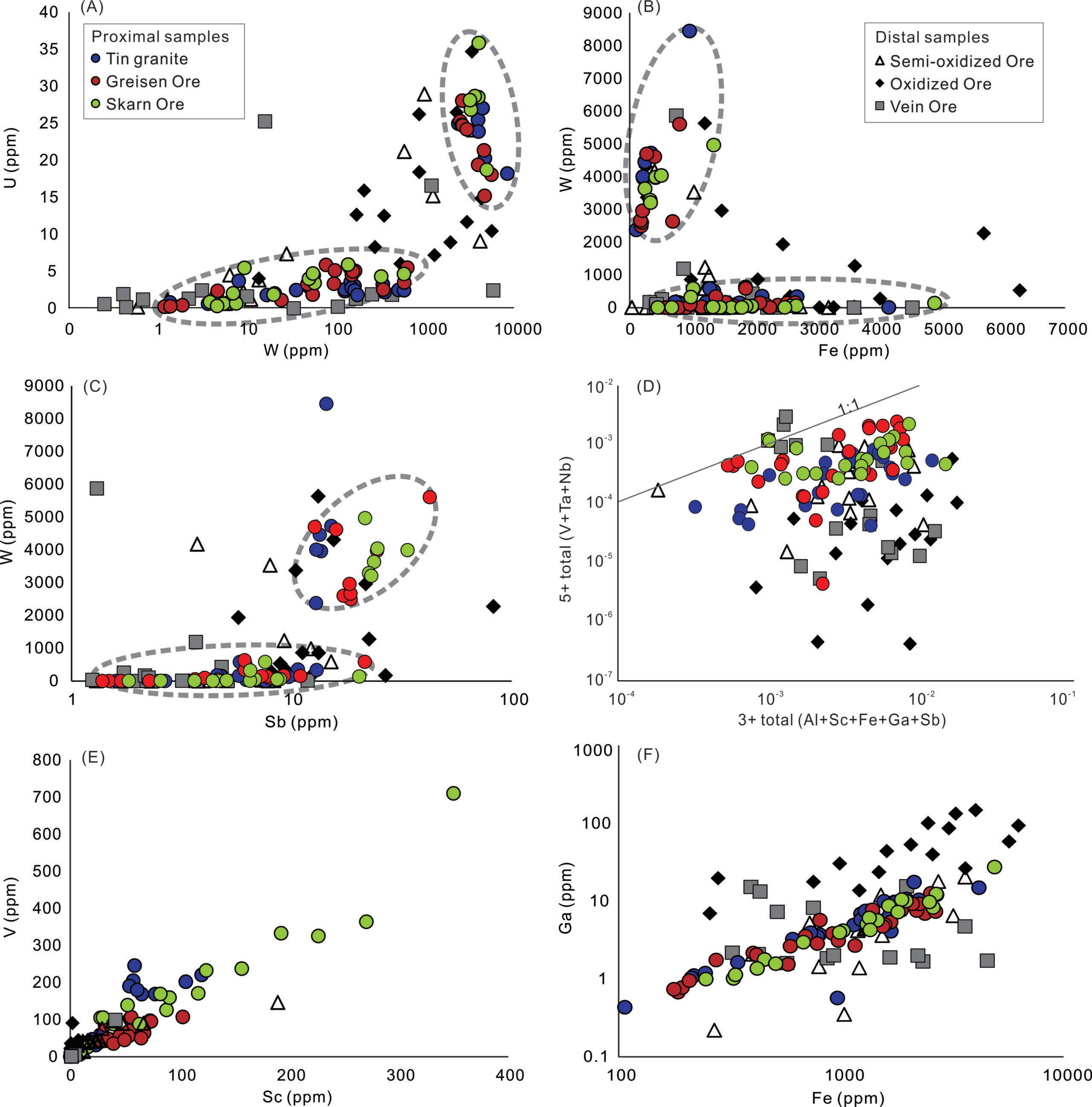
(A)
U (ppm)
W (ppm)
40
35
30
25
20
15
10
5
0
0
1
10
100
1000
10000
Proximal samples
Tin granite
Greisen Ore
Skarn Ore
(B)
W (ppm)
Fe (ppm)
9000
8000
7000
6000
5000
4000
3000
2000
1000
0
1000
2000
3000
4000
5000
6000
7000
Distal samples
Semi-oxidized Ore
Oxidized Ore
Vein Ore
(C)
W (ppm)
Sb (ppm)
1
10
100
(D)
5+ total (V+Ta+Nb)
3+ total (Al+Sc+Fe+Ga+Sb)
1:1
10-2
10-3
10-4
10-5
10-6
10-7
10-4
10-3
10-2
10-1
(E)
V (ppm)
Sc (ppm)
800
700
600
500
400
300
200
100
0
0
100
200
300
400
(F)
Ga (ppm)
Fe (ppm)
1000
100
10
1
0.1
100
1000
10000

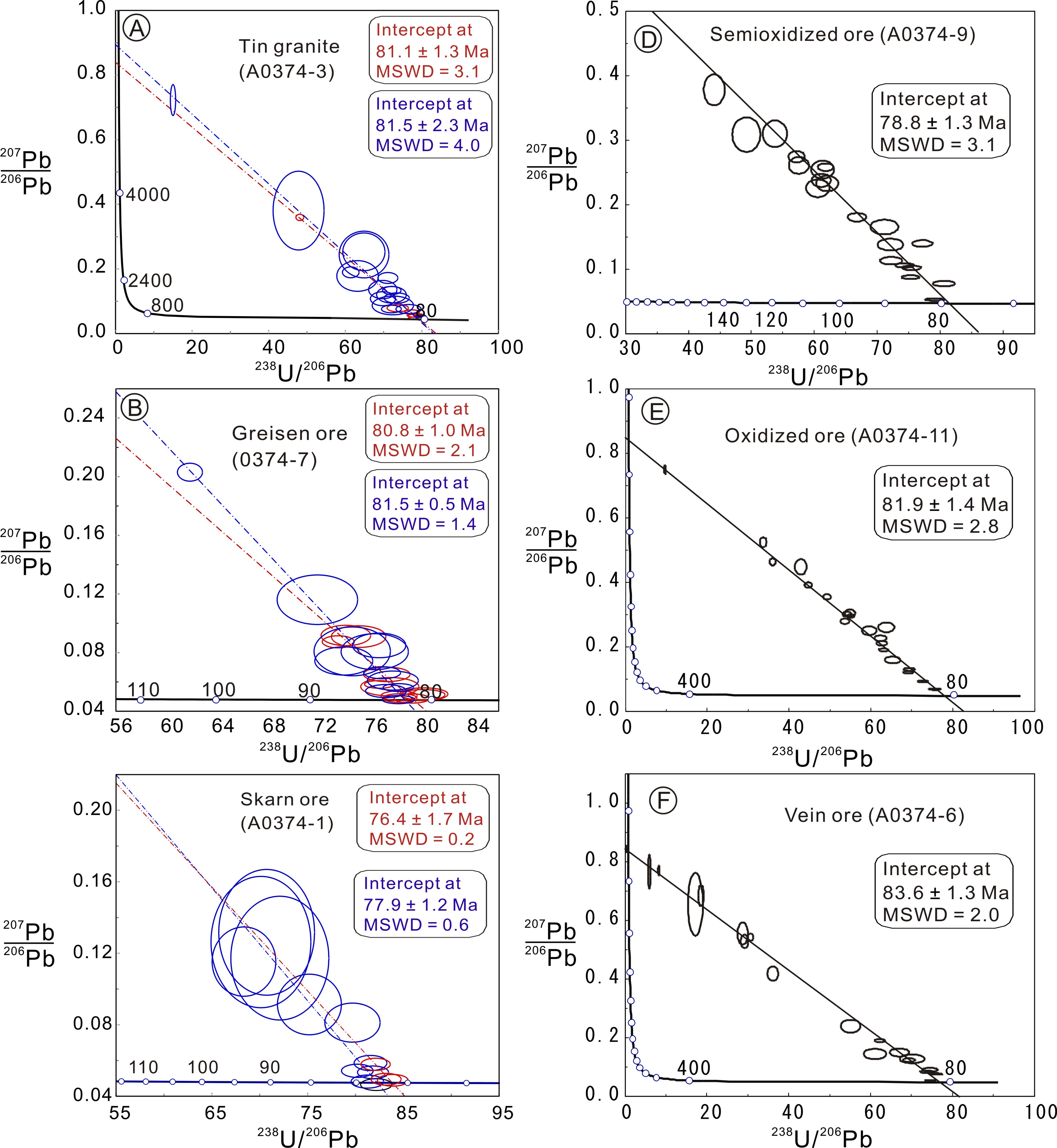
A
Tin granite
(A0374-3)
Intercept at
81.1 ± 1.3 Ma
MSWD = 3.1
Intercept at
81.5 ± 2.3 Ma
MSWD = 4.0
4000
2400
800
80
1.0
0.8
0.6
0.4
0.2
0.0
0
20
40
60
80
100
$^{207}Pb/^{206}Pb$
$^{238}U/^{206}Pb$
D
Semioxidized ore (A0374-9)
Intercept at
78.8 ± 1.3 Ma
MSWD = 3.1
140
120
100
80
0.5
0.4
0.3
0.2
0.1
0.0
30
40
50
60
70
80
90
$^{207}Pb/^{206}Pb$
$^{238}U/^{206}Pb$
B
Greisen ore
(0374-7)
Intercept at
80.8 ± 1.0 Ma
MSWD = 2.1
Intercept at
81.5 ± 0.5 Ma
MSWD = 1.4
110
100
90
80
0.24
0.20
0.16
0.12
0.08
0.04
56
60
64
68
72
76
80
84
$^{207}Pb/^{206}Pb$
$^{238}U/^{206}Pb$
E
Oxidized ore (A0374-11)
Intercept at
81.9 ± 1.4 Ma
MSWD = 2.8
400
80
1.0
0.8
0.6
0.4
0.2
0.0
0
20
40
60
80
100
$^{207}Pb/^{206}Pb$
$^{238}U/^{206}Pb$
Skarn ore
(A0374-1)
Intercept at
76.4 ± 1.7 Ma
MSWD = 0.2
Intercept at
77.9 ± 1.2 Ma
MSWD = 0.6
110
100
90
0.20
0.16
0.12
0.08
0.04
55
65
75
85
95
$^{207}Pb/^{206}Pb$
$^{238}U/^{206}Pb$
F
Vein ore (A0374-6)
Intercept at
83.6 ± 1.3 Ma
MSWD = 2.0
400
80
1.0
0.8
0.6
0.4
0.2
0.0
0
20
40
60
80
100
$^{207}Pb/^{206}Pb$
$^{238}U/^{206}Pb$

Table 1 Brief introduction on the six samples of this study

Sample ID	Locations	Group	Mineral assemblage	Cassiterite characteristics
A0374-1	1860 adit	Skarn ore	Grt, Px, Tr, Chl, Ep, Tur, Cal, Cst, Po, Ccp	Size: 300 x 1250 µm; Euhedral; Regular oscillatory growth CL zoning
A0374-3	1860 adit	Tin granite	K-fsp, Qtz, Ms, Fl, Tur, Cst	Size: 330 x 1380 µm; Euhedral; Regular oscillatory growth CL zoning
A0374-7	Zhuyeshan adit	Greisen ore	Qtz, Ms, Tur, Fl, Cst	Size: 350 x 1300 µm; Euhedral; Regular oscillatory growth CL zoning
A0374-9	1540 adit	Semi-oxidized ore	Lm, Gth, Py, Apy, Gn, Ccp, Cst	Size: 250 x 800 µm; Anhedral; Irregular oscillatory growth CL zoning
A0374-11	1570 adit	Oxidized ore	Hem, OH-Hem, Lm, OH-Gth, Cst, Mlc, Cer	Size: 280 x 600 µm; Anhedral; Irregular oscillatory growth CL zoning
A0374-6	Dadoushan	Vein ore	Grt, Di, Ep, Phl, Brl, Cst, Ccp, Po, Py, Sch	Size: 150 x 500 µm; Anhedral; Irregular oscillatory growth CL zoning

Definitions of mineral abbreviations: Grt-Garnet; Px-Pyroxene; Tr-Tremolite; Chl-Chlorite; Ep-Epi idote; Tur-Tourmaline; Cal-Calcite; Cst-Cassiterite; Po-Pyrrhotite; Ccp-Chalcopyrite; K-fsp-K-feldsp ar; Qtz-Quartz; Ms-Muscovite; Fl-Fluorite; Apy-Arsenopyrite; Gn-Galina; Hem-Heamatite; Phl-Phlo gopite; Sch-Scheelite; Brl-Beryl; Di-Diopside; Cer--Cerussite; Mlc-Malachite; Gth-Goethite; Lm-Li nonite.